The Pennsylvania State University

The Graduate School

# EFFECTIVE USE OF AN ANALYTICAL APPROXIMATION FOR THE RELATIVE MOTION OF SPACECRAFT ON HYPERBOLIC TRAJECTORIES

A Thesis in

Aerospace Engineering

by

Clifford Stueck



Submitted in Partial Fulfillment
of the Requirements
for the Degree of

Master of Science

May 2023

The thesis of Clifford Stueck was reviewed and approved by the following:

Robert G. Melton
Professor of Aerospace Engineering
Thesis Advisor

Puneet Singla
Professor of Aerospace Engineering

Daning Huang
Assistant Professor of Aerospace Engineering

Amy R. Pritchett
Professor of Aerospace Engineering
Head of the Department of Aerospace Engineering

## ABSTRACT

This work assesses the effectiveness of an approximate analytical representation of relative motion between spacecraft on hyperbolic orbits. The relative motion between elliptical orbits has been studied extensively. However, research into the benefits and practicality of using hyperbolic trajectories has not really been explored. An analytical model can prove useful in interplanetary missions involving two or more spacecraft on hyperbolic paths with respect to an object of interest, which can have direct applications to disturbed sensing.

A second-order approximate solution, in spherical coordinates, originally intended for elliptical orbits, is examined for its application to hyperbolas. This solution is formulated in terms of the true anomaly of the chief spacecraft and does not explicitly include time. Thus, a time-explicit representation is sought, and two time-dependent solutions are developed – one that uses a time-dependent series expansion of the hyperbolic anomaly and one that uses a time-dependent series expansion of the trigonometric terms in the second-order solution.

All three solutions are examined. The two time-dependent solutions are found to produce unacceptably large errors in approximating the range between the chief and deputy spacecraft, but the non-time-dependent solution performs very well, with range errors of approximately 2.5%.

# TABLE OF CONTENTS

# LIST OF FIGURES

# LIST OF TABLES

# NOMENCLATURE

| | | |
|---|---|---|
| G | = | Universal Gravitational Constant $\left[\mathrm{N}\left(\frac{\mathrm{m}}{\mathrm{kg}}\right)^2\right]$ |
| m | = | Mass [kg] |
| μ | = | Gravitational Parameter $\left[\frac{\mathrm{km}^3}{\mathrm{s}^2}\right]$ or $\left[\frac{\mathrm{LU}^3}{\mathrm{TU}^2}\right]$ |
| a | = | Semi-Major Axis [km] or [LU] |
| $r_p$ | = | Radius of Periapsis [km] or [LU] |
| p | = | Semi-Latus Rectum [km] or [LU] |
| e | = | Eccentricity |
| h | = | Specific Angular Momentum $\left[\frac{\mathrm{km}^2}{\mathrm{s}}\right]$ or $\left[\frac{\mathrm{LU}^2}{\mathrm{TU}}\right]$ |
| ε | = | Specific Orbital Energy $\left[\frac{\mathrm{km}^2}{\mathrm{s}^2}\right]$ or $\left[\frac{\mathrm{LU}^2}{\mathrm{TU}^2}\right]$ |
| H | = | Hyperbolic Anomaly [radians] |
| f | = | True Anomaly [radians] |
| N | = | Hyperbolic Mean Anomaly [radians] |
| Ω | = | Right Ascension of the Ascending Node [radians] |
| i | = | Inclination [radians] |
| $\vec{r}$ | = | Position Vector [km] or [LU] |
| $\vec{v}$ | = | Velocity Vector $\left[\frac{\mathrm{km}}{\mathrm{s}}\right]$ or $\left[\frac{\mathrm{LU}}{\mathrm{TU}}\right]$ |
| D | = | Relative Distance (Range) [km] or [LU] |
| $\frac{dD}{dt}$ | = | Relative Rate of Change in Distance (Range-Rate) $\left[\frac{\mathrm{km}}{\mathrm{s}}\right]$ or $\left[\frac{\mathrm{LU}}{\mathrm{TU}}\right]$ |
| LU | = | Canonical Distance Unit |
| TU | = | Canonical Time Unit |
| $\hat{X}, \hat{Y}, \hat{Z}$ | = | Cartesian Coordinate Frame Unit Vectors |
| $\hat{I}, \hat{J}, \hat{K}$ | = | Earth-Centered Inertial Coordinate Frame Unit Vectors |

# ACKNOWLEDGEMENTS

I would like to thank my thesis advisor, Dr. Melton, for his indispensable support in establishing and perfecting this thesis. His knowledge of the topic has enabled me to develop a much deeper understanding of orbital mechanics and his suggestions and ideas have always left me wondering what else could be included and done to better my work.

I would also like to thank the Aerospace Department at Penn State for their generous assistantship opportunities that enabled me to return to Penn State and continue my work as a graduate student. The ability to work as a teaching assistant has taught me many valuable lessons that I believe will contribute not only to my success in my career as a researcher and teacher, but also as a member of society in general.

Finally, I would like to thank my family for the all the support they have given me and their never-ending encouragement to study Aerospace Engineering. They have taught me that the world is full uncovered mysteries just waiting to be explored and that when opportunities arise to investigate the unknown, they should be taken. My family has believed in me from the beginning and taught me that even when things get hard there is always a light at the end of the tunnel.

This thesis is dedicated to the ones who stood by my side and believed in me even when nobody else did. The constant encouragement I have received to continue my studies has opened the door to many new opportunities and enabled me to explore a side of aerospace that a few short years ago, I wouldn't have ever considered. Thank you all for being a part of my story.

# Chapter 1

# Introduction

## 1.1 Background

Remote sensing using satellites has been successfully employed in many space missions since the 1960's. Examples include routine meteorological measurements, climate-change observations, Earth-resource assessments, and surface-shape measurements for terrain-mapping. A single large-aperture sensor, such as a telescope, can produce higher resolution images than one with a smaller aperture, but large-aperture sensors can present difficult mechanical challenges (the sensor often has a diameter that exceeds that of the satellite). An alternative approach is to use several smaller-aperture sensors that work simultaneously and whose data are merged to produce measurements or images of a nearly equivalent quality to that of a large-aperture sensor. This approach is called distributed sensing and can make use of the concept of a *synthetic aperture*. It has been used successfully on Earth-orbiting satellites as observed in papers by Barnhart et al [1], and Elderman and Gurfil [2]. A synthetic aperture is possible only if the sensors have fixed relative positions, or at least predictable time-varying relative positions. For space-based distributed sensors, this is accomplished by the use of formation-flying strategies [3]. Such formations have traditionally been achieved by placing satellites in elliptical orbits with slightly different orbital parameters such that the satellites maintain a fixed or slowly varying geometry, with the combined sensors acting as a single large-aperture instrument.

Conventionally, hyperbolic orbits are considered to be escape trajectories because they have a positive energy. Unlike circular or elliptical orbits, the positive energy of hyperbolic trajectories allows objects to escape from a gravitational field (or approach it from infinity) of the

body they are orbiting. Hyperbolic trajectories can be used for flybys of objects of interest such as planets or moons as well as for gravitational assists to increase or decrease a spacecraft's speed. Hyperbolic trajectories can also be used in combination with a planet's gravity field to redirect a spacecraft's path on an interplanetary mission.

The study of hyperbolic trajectories is crucial for understanding the behavior of objects in space, as well as for designing and controlling the motion of spacecraft. In recent years, there has been a growing interest in hyperbolic trajectories in the context of space exploration, as new technologies and mission designs have made it possible to explore more distant and challenging destinations [4]. This includes studies conducted to show how hyperbolic trajectories can be used in conjunction with multiple spacecraft to perform actions around or near celestial bodies [5]. These actions include relaying planetary information, spacecraft coming together to form a distributed sensor, or even spacecraft on different hyperbolic trajectories being used to conduct a survey of the landscape of a body.

### 1.2 Previous Work

Previous work by Stueck [6] used numerical integration to consider the concept of using several satellites as a distributed sensor as they fly by a planet. The primary investigation was geared towards qualifying whether the relative distances between pairs of satellites could remain relatively constant (or at least change slowly during the measurements). The feasibility of this distributed-sensing concept was explored, and numerical methods were used to determine how the range and range-rate of multiple space vehicles could be controlled and limited. This investigation experimented with imposing changes to the classical orbital elements of a trajectory in order to limit the relative motion of spacecraft.

A comparison of different hyperbolic trajectories to find optimal solutions to dealing with a “swarm” of vehicles found that two spacecraft on identical orbits revealed the best possible case for minimizing range-rate [6]. The study revealed that when an inclination or a right ascension of the ascending node (RAAN) change was applied, the range-rate was drastically increased. However, in certain cases the range was decreased, enabling the possibility to minimize the distance by adjusting the inclination and RAAN of the orbits.

A further analysis using three spacecraft on two differently oriented orbits was used to reveal unique trends in the way three spacecraft will move relative to each other. It was shown that a change in inclination utilized the smallest range whereas the RAAN could limit the range-rate between the spacecraft on opposing orbits. This analysis showed there could be opportunity where a combination of inclination, RAAN, and position changes may be able to limit both the range and range-rate between all three vehicles.

### 1.3 Objective

A survey of the literature reveals a substantial body of work devoted to relative motion where one satellite is on a circular orbit and the other on an elliptical orbit, or when both are on elliptical orbits. This history is presented in a survey paper by Sullivan et al [7]. Until relatively recently, all analyses have focused on elliptical orbits, with the equations of motion either linearized (to permit analytic solutions) or formulated in terms of true or eccentric anomaly, forcing an iterative numerical solution. Willis et al [8] developed equations of motion and an approximate solution correct to second order in the relative displacement between two spacecraft. That work focused on the performance of the solution for elliptical orbits and the authors appear to have overlooked an important attribute of the solution: it is not limited to elliptical motion.

Thus, the work done in this thesis is designed to examine the relative error and accuracy that this solution would maintain when it is applied to hyperbolic orbits. The analysis that follows will be used to determine if there is a way to limit this error and understand various trends that appear when a series expansion is used to transform this solution into a function of time. The following study will detail how the model changes for variations in eccentricity, semi-major axis, true anomaly, and time in an attempt to determine if and when the model could be used for such missions that may require distributed sensing technology.

# Chapter 2

# Second-Order Curvilinear Solution

The second-order solution, derived in curvilinear coordinates, for the relative motion of spacecraft on elliptical trajectories was derived by Willis et al [8]. The solution uses a series of transformations to convert relative position ($\delta\vec{r}$) and relative velocity ($\delta\vec{v}$) into spherical coordinates. An outline of the derivation in Ref. [8] is repeated here for completeness.

## 2.1 Chief and Deputy Spacecraft – Equations of Motion

The basic problem considers two spacecraft, a chief and a deputy, operating on different orbits as they travel through space. The chief is taken to be the base spacecraft, serving as the origin of the relative coordinate system, while the deputy spacecraft is defined somewhere in space with its position defined relative to the chief. These spacecraft positions can be defined geometrically as seen in Fig. 2-1. Note that $\theta$ is the angle from $r_c$ to the projection of $r_d$ onto the chief's orbital plane, and $\phi$ is the angle from that projection to $r_d$.

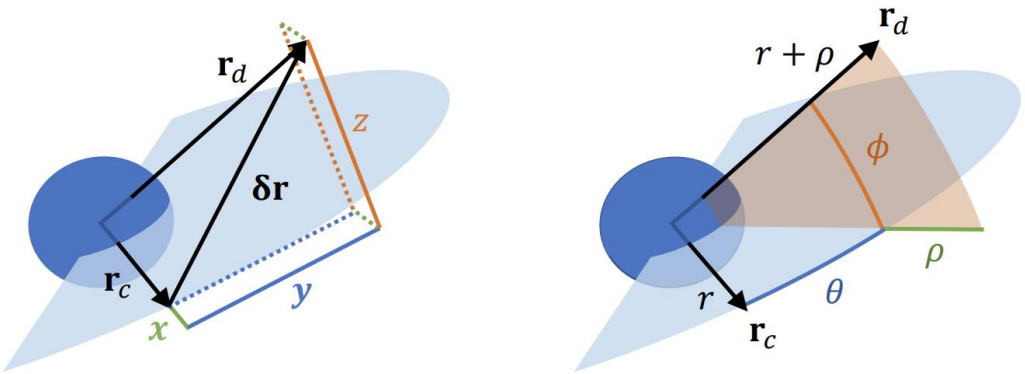


Figure 2-1: Cartesian (Left) and Spherical (Right) Coordinates for Relative Motion [8]

Relative motion between spacecraft on a circular and a slightly elliptical orbit is well understood via the Hill-Clohessy-Wiltshire Equations [9]. In cases where the deputy's distance from the chief is small relative to the chief's orbital radius, it is practical to use Cartesian coordinates to model the relative motion.

By switching to a spherical coordinate system, the relative motion of the spacecraft can be better modelled by taking advantage of the curvilinear geometry of the motion of both spacecraft. The spherical coordinate system is particularly useful in situations where the geometry of the problem has a high degree of symmetry, such as in problems involving spheres, cones, or a rotationally symmetric object. If we define the chief spacecraft as the base orbit and conduct the analysis from the chief to the deputy spacecraft, we are able to create coordinates that capture the difference in radial separation from the central body between the two spacecraft (ρ), the angle of the chief's position vector to the deputy's position vector projected onto the chief's orbital plane (θ), as well as the angle from this projection to the deputy's position vector (ϕ).

Using these relationships, the Cartesian coordinates defining the relative motion between the two spacecraft can be converted to spherical coordinates using

$$\rho = \sqrt{(r+x)^2 + y^2 + z^2} - r$$

$$\theta = \tan^{-1}\left(\frac{y}{r+x}\right)$$

$$\phi = \sin^{-1}\left(\frac{z}{r+\rho}\right) \tag{2-1}$$

$$\dot{\rho} = \frac{(r+x)(\dot{r}+\dot{x}) + y\dot{y} + z\dot{z}}{r+\rho} - r$$

$$\dot{\theta} = \frac{(r+x)\dot{y} - y(\dot{r}+\dot{x})}{(r+x)^2 + y^2}$$

$$\dot{\phi} = \frac{(r+\rho)\dot{z} - z(\dot{r}+\dot{\rho})}{(r+\rho)\sqrt{(r+\rho)^2 - z^2}} \tag{2-2}$$

where $r = \frac{p}{k}$ and $\dot{r} = \sqrt{\frac{\mu}{p}} e \sin f$. To derive the equations of relative motion in spherical coordinates, the acceleration of each spacecraft is defined in an inertial frame. The chief's motion is governed by.

$$\ddot{r}\hat{r}_c + 2\dot{r}\,{}^I\omega^c \times \hat{r}_c + r({}^I\dot{\omega}^c \times \hat{r}_c + {}^I\omega^c \times ({}^I\omega^c \times \hat{r}_c)) = -\frac{\mu}{r^2}\hat{r}_c \tag{2-3}$$

where $\hat{r}_c$ is the unit vector from the central body to the chief's position and ${}^I\omega^c$ is the angular velocity of the chief in the radial-transverse-normal frame with respect to the inertial frame. By assuming no perturbations are present, the vectors can be expressed as $\hat{r}_c = [r, 0, 0]^T$ and ${}^I\dot{\omega}^c = [0, 0, \dot{\theta}_c]$, where $\theta_c$ is the angle from an arbitrary inertially-fixed reference vector in the chief's orbital plane to the chief's position vector $\vec{r}_c$ (Note that the choice of this reference vector and the definition of $\theta_c$ later become irrelevant because only relative coordinates of the deputy spacecraft will be involved). Evaluating Eq. (2-3) leads to the scalar form

$$\ddot{r} - r\dot{\theta}_c = -\frac{\mu}{r^2} \tag{2-4}$$

$$2\dot{r}\dot{\theta}_c + r\ddot{\theta}_c = 0 \tag{2-5}$$

Like Eq. (2-3), the deputy spacecraft's position vector can be described by

$$(\ddot{r} + \ddot{\rho})\hat{r}_d + 2(\dot{r} + \dot{\rho})\,{}^I\omega^d \times \hat{r}_d + (r+\rho)({}^I\dot{\omega}^d \times \hat{r}_d + {}^I\omega^d \times ({}^I\omega^d \times \hat{r}_d)) = -\frac{\mu}{(r+\rho)^2}\hat{r}_d \tag{2-6}$$

The deputy's position vector and angular velocity ($r_d$ and ${}^I\omega^d$) can then be related to the curvilinear coordinates by expressing Eq. (2-6) in the chief's radial-transverse-normal components.

$$r_d = \begin{bmatrix} \cos\phi\cos\theta \\ \cos\phi\sin\theta \\ \sin\theta \end{bmatrix}, \quad {}^I\omega^d = \begin{bmatrix} \dot{\phi}\sin\theta \\ -\dot{\phi}\cos\theta \\ \dot{\theta} + \dot{\theta}_c \end{bmatrix}, \quad {}^I\dot{\omega}^d = \begin{bmatrix} \ddot{\phi}\sin\theta + (\dot{\theta} + \theta_c)\dot{\phi}\cos\theta \\ -\ddot{\phi}\cos\theta + (\dot{\theta} + \dot{\theta}_c)\dot{\phi}\sin\theta \\ \ddot{\theta} + \ddot{\theta}_c \end{bmatrix} \tag{2-7}$$

By substituting Eq. (2-7) into Eq. (2-6) and solving for $\ddot{\rho}, \ddot{\theta}, \text{and } \ddot{\phi}$, the following exact second-order equations of relative motion result is obtained:

$$\ddot{\rho} = -\ddot{r} - \frac{\mu}{(r+\rho)^2} + (r+\rho)\left(\dot{\phi}^2 + \left(\dot{\theta}+\dot{\theta}_c\right)^2 \cos^2\phi\right)$$

$$\ddot{\theta} = -\ddot{\theta}_c + 2\left(\dot{\theta}+\dot{\theta}_c\right)\dot{\phi}\tan\phi - 2\frac{(\dot{r}+\dot{\rho})}{(r+\rho)}\left(\dot{\theta}+\dot{\theta}_c\right)$$

$$\ddot{\phi} = -2\frac{(\dot{r}+\dot{\rho})}{(r+\rho)}\dot{\phi} - \left(\dot{\theta}+\dot{\theta}_c\right)^2 \cos\phi \sin\phi$$

(2-8)

The right-hand side of Eq. (2-8) can then be expanded to second order in the state variables $(\rho, \theta, \phi, \dot{\rho}, \dot{\theta}, \dot{\phi})$ to get

$$\ddot{\rho} = 2\frac{\mu}{r^3}\rho - 3\frac{\mu}{r^4}\rho^2 + \rho\dot{\theta}_c^2 + 2r\dot{\theta}_c\dot{\theta} + r\dot{\phi}^2 + 2\dot{\theta}_c\rho\dot{\theta} + r\dot{\theta}^2 - r\dot{\theta}_c^2\phi^2$$

$$\ddot{\theta} = -\frac{1}{r}\left(\rho\ddot{\theta}_c + 2\dot{\rho}\dot{\theta}_c + 2\dot{r}\dot{\theta} + 2\dot{\rho}\dot{\theta} - 2r\dot{\theta}_c\dot{\phi}\phi - \frac{\ddot{\theta}_c}{r}\rho^2 - 2\frac{\dot{\theta}_c}{r}\rho\dot{\rho} - 2\frac{\dot{r}}{r}\rho\dot{\theta}\right)$$

$$\ddot{\phi} = -\frac{1}{r}\left(r\dot{\theta}_c^2\phi + 2\dot{r}\dot{\phi} + 2r\dot{\theta}_c\dot{\theta}\dot{\phi} + 2\dot{\rho}\dot{\phi} - 2\frac{\dot{r}}{r}\rho\dot{\phi}\right)$$

(2-9)

### 2.2 Second-Order Approximate Solution

Willis et al. [8] then uses the method of successive approximations (also known as Picard Iteration [10]) to approximate the solution to Eq. (2-9) in the form

$$\begin{bmatrix}\tilde{\rho}\\ \theta\\ \phi\end{bmatrix} = \begin{bmatrix}\tilde{\rho}_1\\ \theta_1\\ \phi_1\end{bmatrix} + \begin{bmatrix}\tilde{\rho}_2\\ \theta_2\\ \phi_2\end{bmatrix} + \cdots \tag{2-10}$$

where $\tilde{\rho} = \frac{\rho}{r}$ and the terms $\tilde{\rho}_1, \theta_1, \phi_1$ approximate the solution to first order in $\frac{\delta r}{r}$ and $\tilde{\rho}_2, \theta_2, \phi_2$ add corrective terms to order $\left(\frac{\delta r}{r}\right)^2$. The method of successive approximations converts a first-order ordinary differential equation of the form

$$\dot{\underline{x}} = \underline{f}(\underline{x}, t), \underline{x}(t_0) = x_0 \tag{2-11}$$

into a recursive integral equation

$$\underline{x}_{j+1} = \underline{x_0} + \int_{t_0}^{t} \underline{f}(\underline{x}_j(t), s)\, ds \tag{2-12}$$

where $\underline{x}$ is the matrix of state variables (a system of m second-order differential equations can be converted to a set of 2m first order equations by suitable definitions of the state variables). The approximate solution is then truncated after the j = 1 term. Willis et al [8] made use of the first-order solution (j = 0), developed earlier by Yamanaka and Ankersen [11], to arrive at a more compact form in the next recursion giving the second-order solution

$$\begin{aligned}\rho = {} & K_1\left(1 - \frac{3}{2}ekJ(t)\sin f\right) + K_2 k\sin f + K_3 k\cos f + c_{\rho j}\left(1 - \frac{3}{2}ekJ(t)\sin f\right) + c_{\rho s}k\sin f \\ & + c_{\rho c}k\cos f + K_1^2\left(\frac{1}{4} + \frac{9}{8}k^3J(t)^2 e\cos f\right) - \frac{3}{2}(K_1K_2\cos f - K_1K_3\sin f)k^3J(t) \\ & + \mathrm{K}_2^2\left[\left(-\frac{\mathrm{e}^2}{2}\sin^2 f + \frac{3}{2}(\mathrm{k}-1) + \frac{1}{1-\mathrm{e}^2}\right)\cos^2 f + \frac{\mathrm{e}(1+\mathrm{e}^2)\cos f}{2(1-e^2)}\right] \\ & + \mathrm{K}_2\mathrm{K}_3\frac{(\mathrm{ek}^2 - (1+\mathrm{k})\cos f)\,\mathrm{k}\sin f}{1-e^2} + \mathrm{k}_3^2\frac{\mathrm{k}\left(3 - \mathrm{k} - \mathrm{k}^2 + \mathrm{k}^3 - (1+\mathrm{k})(\mathrm{e}^2 + \cos^2 f)\right)}{2(1-e^2)}\end{aligned}$$

$$\theta = K_4 + K_2(1+k)\cos f - K_3(1+k)\sin f - \frac{3}{2}K_1 k^2 J(t)$$
$$+ \left(c_{\rho s} - K_1 K_2\right)\left((1+k)\cos f - (1+k_0)\cos f_0\right) - \frac{3}{2}\left(K_1^2 - K_1 K_3 e - c_{\rho j}\right) k^2 J(t)$$
$$+ \left(K_1 K_3 - K_2^2 \frac{e^3}{2(1-e^2)} - c_{\rho c}\right)\left((1+k)\sin f - (1+k_0)\sin f_0\right)$$
$$+ K_1^2\left(-\frac{9}{4} e k^3 J(t)^2 \sin f\right) + 3\left(K_1 K_2 \sin f + K_1 K_3 \cos f\right) k^3 J(t)$$
$$+ (K_3^2 - K_2^2)\left[\left(\frac{\cos f + 2e}{2(1-e^2)} + \mathrm{k}(1+\mathrm{k})\cos f\right)\sin f\right.$$
$$\left. - \left(\frac{\cos f_0 + 2e}{2(1-e^2)} + \mathrm{k}_0(1+\mathrm{k}_0)\cos f_0\right)\sin f_0\right]$$
$$+ \mathrm{K}_2\mathrm{K}_3\left[\left(\mathrm{k}^2 + \frac{\mathrm{k}^2}{1-e^2} - (1 + 2\mathrm{k} + 2\mathrm{k}^2)\cos^2 f\right)\right.$$
$$\left. - \left(\mathrm{k}_0^2 + \frac{\mathrm{k}_0^2}{1-e^2} - (1 + 2\mathrm{k}_0 + 2\mathrm{k}_0^2)\cos^2 f_0\right)\right] + \mathrm{K}_3^2\mathrm{e}\left(\sin f - \sin f_0\right) + \frac{1}{4}(\mathrm{K}_6^2$$
$$- \mathrm{K}_5^2)(\sin 2f - \sin 2f_0) + \mathrm{K}_5\mathrm{K}_6(\sin^2 f - \sin^2 f_0)$$

$$\phi = K_5 \sin f + K_6 \cos f + \frac{3}{2}(K_1 K_6 \sin f - K_1 K_5 \cos f)\, k^2 J(t)$$
$$+ \frac{3}{2}(K_1 K_5 \cos f_0 - K_1 K_6 \sin f_0)\sin(f - f_0)$$
$$+ 2\left((K_2 K_5 - K_3 K_6)\cos f_0 - (K_2 K_6 + K_3 K_5)\sin f_0\right) k_0 \sin f_0 \sin(f - f_0)$$
$$+ K_2 K_5\left((1+k)\cos f - (1+k_0)\cos f_0\right)\cos f$$
$$- (K_2 K_6 + K_3 K_5)\left((1+k)\cos f - (1+k_0)\cos f_0\right)\sin f + K_3 K_6((1+k)\sin^2 f$$
$$- e\sin^2 f_0 \cos f - 2\sin f_0 \sin f)$$

(2-13)

where k = 1 + e cos(f) and the $K_i$, which depend on the initial conditions of the chief and the deputy, are given by

$$\begin{bmatrix} K_1 \\ K_2 \\ K_3 \\ K_4 \\ K_5 \\ K_6 \end{bmatrix} = \begin{bmatrix} \frac{6k_0 + 2e^2 - 2}{1-e^2} & 0 & 0 & \frac{2ek_0 \sin f_0}{1-e^2} & \frac{2k_0^2}{1-e^2} & 0 \\ -3\left(1 + \frac{e^2}{k_0}\right)\frac{\sin f_0}{1-e^2} & 0 & 0 & \frac{k_0 \cos f_0 - 2e}{1-e^2} & -\frac{1+k_0}{1-e^2}\sin f_0 & 0 \\ -3\frac{e + \cos f_0}{1-e^2} & 0 & 0 & -\frac{k_0 \sin f_0}{1-e^2} & -\frac{e + (1+k_0)\cos f_0}{1-e^2} & 0 \\ -3e\left(1 + \frac{1}{k_0}\right)\frac{\sin f_0}{1-e^2} & 1 & 0 & \frac{ek_0 \cos f_0 - 2}{1-e^2} & -e\frac{1+k_0}{1-e^2}\sin f_0 & 0 \\ 0 & 0 & \sin f_0 & 0 & 0 & \cos f_0 \\ 0 & 0 & \cos f_0 & 0 & 0 & -\sin f_0 \end{bmatrix} \begin{bmatrix} \tilde{\rho} \\ \theta \\ \phi \\ \tilde{\rho}' \\ \theta' \\ \phi' \end{bmatrix}_0 \tag{2-14}$$

And the $c_{\rho j}, c_{\rho s}$, and $c_{\rho c}$ are

$$c_{\rho j} = \sum_i \sum_{k \geq i} c_{\rho jik} \tag{2-15}$$

$$c_{\rho j11} = \frac{1}{2} K_1^2 \left(1 - 3k_0 \frac{1 + 2k_0}{1 - e^2}\right)$$

$$c_{\rho j12} = -K_1 K_2 \frac{3 + 7k_0}{1 - e^2} k_0^2 \sin f_0$$

$$c_{\rho j13} = K_1 K_3 \frac{2e - (3 + 7k_0)\cos f_0}{1 - e^2} k_0^2$$

$$c_{\rho j22} = K_2^2 \frac{k_0 - 2(1 + 2k_0)\sin^2 f_0}{1 - e^2} k_0^3$$

$$c_{\rho j23} = -2K_2 K_3 \frac{1 + 2k_0}{1 - e^2} k_0^3 \sin 2f_0$$

$$c_{\rho j33} = K_3^2 \frac{e^2 + k_0^2 - 2k_0(1 + 2k_0)\cos^2 f_0}{1 - e^2} k_0^2$$

$$c_{\rho j55} = K_5^2 \frac{k_0^2}{1 - e^2} \cos 2f_0$$

$$c_{\rho j56} = -2K_5 K_6 \frac{k_0^2}{1 - e^2} \sin 2f_0$$

$$c_{\rho j66} = -K_6^2 \frac{k_0^2}{1 - e^2} \cos 2f_0$$

$$c_{\rho s} = \sum_i \sum_{k \geq i} c_{\rho sik} \tag{2-16}$$

$$c_{\rho s11} = \frac{3}{4} K_1^2 \frac{3k_0 + 2k_0^2 + e^2}{k_0(1-e^2)} \sin f_0$$

$$c_{\rho s12} = K_1 K_2 \frac{6 - 3k_0 + (10 + 7k_0)\sin^2 f_0}{2(1-e^2)} k_0$$

$$c_{\rho s13} = K_1 K_3 \frac{e(k_0 - 5) + (10 + 7k_0)k_0 \cos f_0}{2(1-e^2)} \sin f_0$$

$$c_{\rho s22} = K_2^2 \frac{9 + k_0 - 2(3 + 2k_0)\cos^2 f_0}{2(1-e^2)} k_0^2 \sin f_0$$

$$c_{\rho s23} = K_2 K_3 \frac{e k_0(k_0 - 2) + (1 - k_0 + 10k_0^2 + 2k_0^3)\cos f_0 - 2k_0^2(3 + 2k_0)\cos^3 f_0}{2(1-e^2)}$$

$$c_{\rho s33} = K_3^2 \frac{-2 - e^2(k_0 - 1) + 2k_0 - 5k_0^2 + k_0^3 + 2k_0^2(3 + 2k_0)\cos^2 f_0}{2(1-e^2)} \sin f_0$$

$$c_{\rho s55} = -K_5^2 \frac{\cos 2f_0}{2(1-e^2)} (1 + k_0) \sin f_0$$

$$c_{\rho s56} = K_5 K_6 \frac{\sin 2f_0}{1-e^2} (1 + k_0) \sin f_0$$

$$c_{\rho s66} = K_6^2 \frac{\cos 2f_0}{2(1-e^2)} (1 - k_0) \sin f_0$$

$$c_{\rho c} = \sum_i \sum_{k \geq i} c_{\rho cik} \tag{2-17}$$

$$c_{\rho c11} = \frac{3}{4} K_1^2 \frac{(3 + 2k_0)\cos f_0 + 3e}{1 - e^2}$$

$$c_{\rho c12} = K_1 K_2 \frac{(10 + 7k_0)\cos f_0 + 10e}{2(1-e^2)} k_0 \sin f_0$$

$$c_{\rho c13} = K_1 K_3 \left( \frac{5}{2} - \frac{10 + 7k_0}{2(1-e^2)} k_0 \sin^2 f_0 + \frac{15}{2(1-e^2)} k_0^2 \right)$$

$$c_{\rho c22} = -K_2^2 \frac{e^3 + 2(3 + 2k_0)k_0^2 \cos^3 f_0 + 2e(1 - 3k_0^2) + (1 + k_0 - 11k_0^2 + 3k_0^3)\cos f_0}{2(1-e^2)}$$

$$c_{\rho c23} = 2K_2 K_3 \frac{(1-e^2) - 3k_0(1 - k_0) + k_0(3 + 2k_0)\cos^2 f_0}{1 - e^2} k_0 \sin f_0$$

$$c_{\rho c33} = K_3^2 \frac{e k_0 (4 - 5k_0) + (-1 + 3k_0 - 7k_0^2 + 5k_0^3)\cos f_0 + 2(3 + 2k_0)k_0^2 \cos^3 f_0}{2(1 - e^2)}$$

$$c_{\rho c55} = -K_5^2 \frac{e + (1 + k_0)\cos f_0}{2(1 - e^2)} \cos 2f_0$$

$$c_{\rho c56} = K_5 K_6 \frac{e + (1 + k_0)\cos f_0}{1 - e^2} \sin 2f_0$$

$$c_{\rho c66} = K_6^2 \frac{e + (1 + k_0)\cos f_0}{2(1 - e^2)} \cos 2f_0$$

The aforementioned equations provide the basis for the analytical solution to the relative motion between the chief and deputy spacecraft. For more details on the derivation of the second-order solution and its constants and coefficients, refer to Ref [8].

# Chapter 3

# Numerical Solution for Hyperbolic Trajectories

Orbital mechanics involves finding ways to study objects in space moving under the influence of forces such as gravity, atmospheric drag, thrust, etc. To study the relative position of spacecraft and speed between two or more spacecraft on hyperbolic paths, an analysis of different trajectories is explored. This exploration typically uses numerical solutions as a means of estimating the position and velocity of a space vehicle as the equations governing the motion of objects in space can be highly complex and difficult to solve analytically. Numerical methods provide a practical means to simulate and analyze the motion of spacecraft and other objects in orbit.

## 3.1 Parameter Definition

The resulting work makes use of canonical units, which are a system of units used to simplify the measurement of physical quantities. Canonical units are very useful when the precise distances and masses of objects in space are not readily available. In the case of this study, canonical units are implemented to create a general exploration of the motion around any particular body. The primary units in this work define a planetary radius as the length unit (LU)

$$r_{planet} = LU \tag{3-1}$$

with a gravitational parameter of a general body equivalent to Eq. (3-2).

$$\mu = 4\pi^2 \frac{LU^3}{TU^2} \tag{3-2}$$

This then leads to the definition of the TU as the orbital period of a circular orbit with a radius of 1 LU.

$$Orbital\ Period = \ TU = 2\pi\sqrt{\frac{r_{planet}^3}{\mu}} = 2\pi\sqrt{\frac{1\ LU^3}{\mu}} \tag{3-3}$$

### 3.2 Hyperbolic Trajectories

Hyperbolic trajectories can be identified by their geometric qualities and dynamic behavior with the idea being that a body traveling along this trajectory will coast towards infinity, settling to a final non-zero (excess) velocity relative to the central body. Like an elliptical orbit, a hyperbolic trajectory for a given system can be defined by its semi-major axis and eccentricity. The main characteristics of these trajectories include a value less than zero for their semi major axis, a value greater than one for their eccentricity, and a value greater than zero for their energy. These features are unique to this style of orbit. This is further represented geometrically as seen in Fig. 3-1.

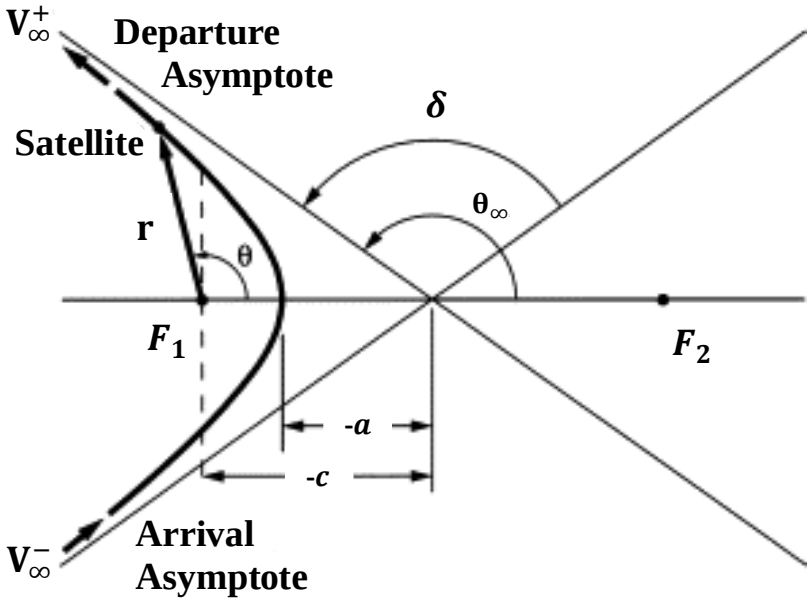


Figure 3-1: Geometric Significance of a Hyperbolic Trajectory [15]

where F is the focus of the conic, r is the position vector of the spacecraft, θ describes where the spacecraft is located on the orbit, $V_\infty$ represents the hyperbolic excess velocity with the positive superscript denoting departure and the minus sign denoting arrival, δ is the angle between the departure and the arrival asymptotes, and $\theta_\infty$ is the true anomaly as the trajectory goes to infinity. The quantity a is used to represent the semi-major axis of the orbit. It should also be noted that in Fig. 3-1, -c = -ae where e is the eccentricity of the hyperbola.

### 3.3 Hyperbolic Time Equation

In a typical problem where knowledge of the position of a spacecraft on a hyperbolic trajectory at a given time is desired, the hyperbolic anomaly (H) can be calculated using the relationship

$$\sqrt{\frac{\mu}{-(a)^3}}(t - t_o) = e\sinh H - H \tag{3-4}$$

where μ is the gravitational parameter of the celestial body, a is the semi-major axis of the orbit, and $t_o$ is the epoch time or a reference time to which the orbital elements are referred. The relationship between H and the true anomaly of the spacecraft (f) is

$$\tan\frac{f}{2} = \sqrt{\frac{e+1}{e-1}}\tanh\frac{H}{2} \tag{3-5}$$

however, there is no closed-form solution for H in Eq. (3-4). This means that in order to compute the position of the spacecraft on a hyperbolic trajectory for a given time, t, one must solve Eq. (3-4) either by numerical iteration or by employing a Lagrange series expansion of the hyperbolic anomaly.

The work that follows will explore the error in spherical coordinates when comparing the numerical solution to the analytical approximation (via series expansion). Since the numerical

solutions are stable and accurate, they are considered to be the ‘true” solution to the equations of motion.

### 3.4 Numerical Integration

Runge-Kutta methods are suitable for conducting analysis of multiple hyperbolic trajectories simultaneously. ODE45 is a built-in function in MATLAB based on an explicit Runge-Kutta formula that computes the position at the current time using only the position from the previous time step and derivative information from the equations of motion [12]. ODE45 will be used to simultaneously integrate multiple trajectories in order to compare the relative distance (range) and its time-derivative (range-rate) and the relative spherical coordinates of satellites on different three-dimensional hyperbolic trajectories.

The equations of motion that will be used for the integration of the deputy and chief spacecraft’s coordinates are defined as

$$\ddot{r} - r\dot{\theta}_c^2 = -\frac{\mu}{r^2}$$

$$2\dot{r}\dot{\theta}_c + r\ddot{\theta}_c = 0$$

$$\ddot{\rho} = -\ddot{r} - \frac{\mu}{(r+\rho)^2} + (r+\rho)\left(\dot{\phi}^2 + \left(\dot{\theta} + \dot{\theta}_c\right)^2 \cos^2\phi\right)$$

$$\ddot{\theta} = -\ddot{\theta}_c + 2\left(\dot{\theta} + \dot{\theta}_c\right)\dot{\phi}\tan\phi - 2\frac{\dot{r} + \dot{\rho}}{r+\rho}\left(\dot{\theta} + \dot{\theta}_c\right)$$

$$\ddot{\phi} = -2\frac{(\dot{r} + \dot{\rho})}{(r+\rho)}\dot{\phi} - \left(\dot{\theta} + \dot{\theta}_c\right)^2 \cos\phi \sin\phi$$

(3-6)

where the ρ, θ, and ϕ coordinates represent the deputy spacecraft with respect to the chief and the r and $\theta_c$ coordinates represent the radial location and true anomaly of the chief spacecraft. Once

the integration has been performed, the values for r, $\theta_c$, ρ, θ, and ϕ can then be used to estimate the error between the numerical and analytical solutions in terms of ρ and θ.

$$\%\ Error\ in\ \rho = \frac{\rho_{analytical} - \rho_{numerical}}{\rho_{numerical}} \times 100 \tag{3-7}$$

$$\%\ Error\ in\ \theta = \frac{\theta_{analytical} - \theta_{numerical}}{\theta_{numerical}} \times 100 \tag{3-8}$$

where $\rho_{analytical} = \tilde{\rho} \cdot r_{chief}$. By converting the spherical coordinates back into a Cartesian coordinate system, the range approximation can also be observed. The x, y, and z relative coordinates could be calculated with both numerical and analytical results using equation (3-9).

$$\begin{gathered} \delta x = (r + \rho)\cos\phi\cos\theta - r \\ \delta y = (r + \rho)\cos\phi\sin\theta \\ \delta z = (r + \rho)\sin\phi \end{gathered} \tag{3-10}$$

These equations can then be combined to give the total range magnitude between the two vehicles.

$$range = \sqrt{\delta x^2 + \delta y^2 + \delta z^2} \tag{3-11}$$

Finally, in the same manner as equations (3-12) and (3-13), the percent error in range could be determined

$$\%\ Error\ in\ Range = \frac{Range_{analytical} - Range_{numerical}}{Range_{numerical}} \times 100 \tag{3-14}$$

# Chapter 4

# Time-Dependent Solution for True Anomaly

The approximate solution in Eqs. (2-13) is in terms of true anomaly f. A more useful form for mission planning (and controller design for the formation-flying needed for distributed sensing) would be a solution with time t as the independent variable. No closed-form relationship between f and t exists; however, an approximation is possible. The idea is to create a series expansion of the hyperbolic anomaly as a function of a variable that is linear in time, and then substitute that expression into expressions for the sinf, cosf, and sin2f terms that appears in Eqs. (2-13) in order to derive a true analytical solution. This new equation for true anomaly would enable the study of the accuracy of a time dependent series expansion when applied to hyperbolic trajectories.

## 4.1 Lagrange Expansion of Hyperbolic Anomaly

In order to derive a time dependent solution for the true anomaly of an orbit, the hyperbolic time equation must be considered. By manipulating Eq. (3-4), it can be shown that

$$H = -N + e \sinh H \tag{4-1}$$

where N represents the hyperbolic mean anomaly of the body in question and corresponds to

$$N = \sqrt{\frac{\mu}{a^3}}(t - t_0) \tag{4-2}$$

Since N is a linear function of t, this results in a time dependent solution for the hyperbolic anomaly.

The next step is to apply Lagrange series expansion theorem. This technique can be applied only to equations bearing the form

$$y = x + \alpha f(y) \tag{4-3}$$

The derivation of the basic Lagrange expansion theorem [10] can be shown by expanding y(x, α) about α = 0 in a Taylor series.

$$y(x,\alpha) = y(x,0) + \alpha \frac{\partial y}{\partial \alpha}\Big|_{\alpha=0} + \frac{\alpha^2}{2}\frac{\partial^2 y}{\partial \alpha^2}\Big|_{\alpha=0} + \cdots \tag{4-4}$$

It is then easy to see that

$$y(x,0) = x$$

$$\frac{\partial y}{\partial \alpha}(x,\alpha) = f(y) + \alpha \frac{df}{dy}\frac{\partial y}{\partial \alpha}$$

Therefore, the first two derivatives of the Taylor series can be produced and proven to be the following:

1st Derivative:

$$\frac{\partial y}{\partial \alpha}\Big|_{\alpha=0} = f(y) = f[x + 0 \cdot f(y)] = f(x) \tag{4-5}$$

2nd Derivative:

$$\frac{\partial^2 y}{\partial \alpha^2} = \frac{df}{dy}\frac{\partial y}{\partial \alpha} + \frac{\partial \alpha}{\partial \alpha}\frac{df}{dy}\frac{\partial y}{\partial \alpha} + \alpha\left[\frac{d^2 f}{dy^2}\left(\frac{\partial y}{\partial \alpha}\right)^2 + \frac{df}{dy}\frac{\partial^2 y}{\partial \alpha^2}\right]$$

$$= 2f(y)\frac{df}{dy}\Big|_{y=x} = \frac{d}{dx}[f^2(x)] \tag{4-6}$$

This pattern continues for higher order derivatives. Finally, by using this derivation and taking hyperbolic anomaly H to be y, hyperbolic mean anomaly -N to be x, eccentricity e to be α, and f(y) to be sinh(H), a series expansion of the hyperbolic anomaly H can be implemented. Thus, the Lagrange expansion was computed using the following derived formula:

$$y = x + \sum_{n=1}^{\infty} \frac{\alpha^n}{n!} \frac{d^{n-1}}{dx^{n-1}} [f^n(x)] \tag{4-7}$$

Lagrange generalized Eq. (4-7) by creating the Lagrange generalized series expansion theorem, which enables any function F(y) to be expanded as a power series in $\alpha$. With y defined in Eq. (4-3), then

$$F(y) = F(x) + \sum_{n=1}^{\infty} \frac{\alpha^n}{n!} \frac{d^{n-1}}{dx^{n-1}} \left[ \phi(x)^n \frac{dF(x)}{dx} \right] \tag{4-8}$$

where F(y) is any function, F(x) is that same function applied to the independent variable, $\phi(x)$ is the sinh function in Eq. (4-1), and $\alpha$ is considered to be a small parameter. In the case of hyperbolic motion $\alpha = e$, which is greater than unity, so the series will not converge; however, it may provide a useful approximation if truncated. A critical feature of the expansions in Eqs. (4-7) and (4-8) is that they are in terms of x = -N, which is explicit in time t. This makes it possible to approximate the solution to the hyperbolic time relation, Eq. (4-1) without the need for numerical iteration.

By applying Eqs. (4-7) or (4-8), a second-order and third-order solution to the hyperbolic anomaly can be derived

$$H_{2nd} = -N + e \sinh(N) + e^2 \sinh(N) \cosh(N) \tag{4-9}$$

$$H_{3rd} = -N + e \sinh(N) + e^2 \sinh(N) \cosh(N) + \frac{e^3}{2} (\sinh^3(N) + 2 \cosh^2(N) \sinh(N)) \tag{4-10}$$

although it must be noted that this expansion clearly does not converge since e > 1 for hyperbolic paths. Nevertheless, the approximation may prove useful within limited ranges of e and N.

Since equations (4-9) and (4-10) demonstrate that as the expansion is continued, the eccentricity increases in order of magnitude, only the second order and third order solutions were tested. This is because with hyperbolic trajectories the eccentricity is greater than one, which

implies that as the expansion is continued, the solution will continue to diverge away from the actual values of hyperbolic anomaly.

# Chapter 5

# Applying the Analytical Model Without Time Dependence

To understand how the analytical model functions without a series expansion of the hyperbolic anomaly, test cases of the analytical model applied over a range of eccentricities and true anomalies were explored.

## 5.1 Initial Conditions and Setup

To understand how well the model works, a wide range of eccentricities and initial true anomalies of the chief spacecraft were studied. True anomaly was studied from 0 to 100 degrees while the eccentricity was chosen to be from 1.2 to 5. Since it was already shown by Melton [13] that as the model approaches e = 1, it begins to rapidly increase in error [13], the eccentricity range was started from 1.2 to limit this expected initial error. By holding the radius of periapsis constant at 1.2 LU, the semi-major axis of the studied range could be calculated by means of the orbit equation for every eccentricity:

$$a = \frac{r_p}{1 - e} \tag{5-1}$$

The initial conditions for the model were chosen as shown in Table 5-1. It should be noted that these initial conditions with $z_0 = \dot{z}_0 = 0$ imply only two-dimensional motion, i.e., the deputy will move in the same plane as the chief. All of the studies in this thesis consider only this type of in-plane relative motion. Errors in approximating out-of-plane motion are expected to be of lower magnitude (similar to the well-known behavior for elliptical orbits).

Table 5-1: Analytical Model Initial Conditions

| **Parameter:** | **Initial Input:** | **Parameter:** | **Initial Input** |
|---|---|---|---|
| P | $a(1-e^2)$ | $x_0$ | 0.0000784 LU |
| $\boldsymbol{f_0}$ | 0 | $y_0$ | 0 |
| $\boldsymbol{t_0}$ | 0 | $z_0$ | 0 |
| $\boldsymbol{k_0}$ | $1 + e\cos f_0$ | $\dot{x}_0$ | 0 |
| $\boldsymbol{r_0}$ | $r_p$ | $\dot{y}_0$ | 0 |
| $\boldsymbol{v_0}$ | $\sqrt{2\left(E + \frac{\mu}{r_0}\right)}$ | $\dot{z}_0$ | 0 |
| $\dot{\boldsymbol{r}}_{\boldsymbol{0}}$ | $\sqrt{\frac{\mu}{p}}\, e \sin f_0$ | | |

## 5.2 Observations

A study of error in θ, ρ, and range r was conducted, producing the results shown in Figs. 5-1 – 5-4.

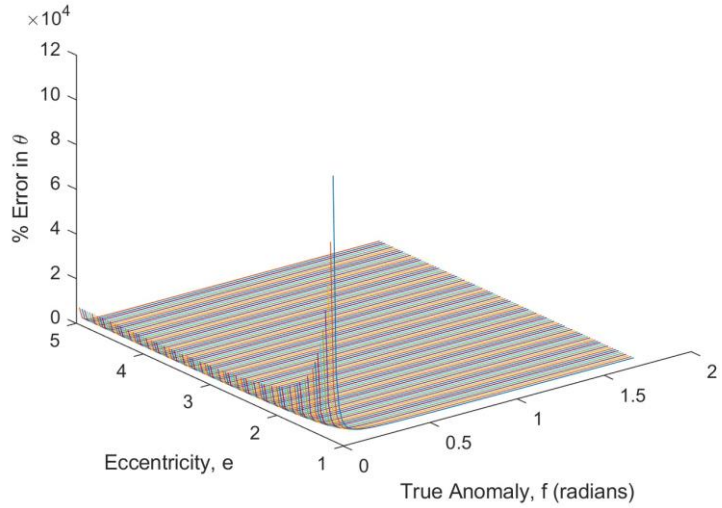


Figure 5-1: Error in θ for Eccentricity-Anomaly Study

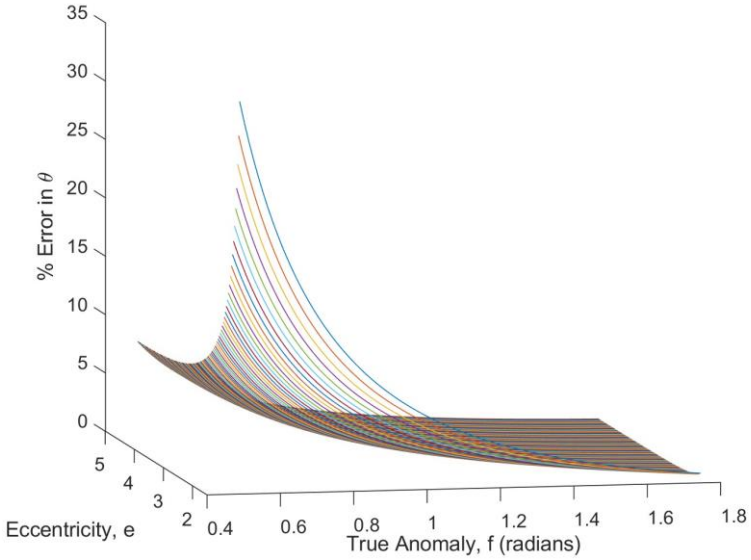


Figure 5-2: Expanded View of Figure 5-1

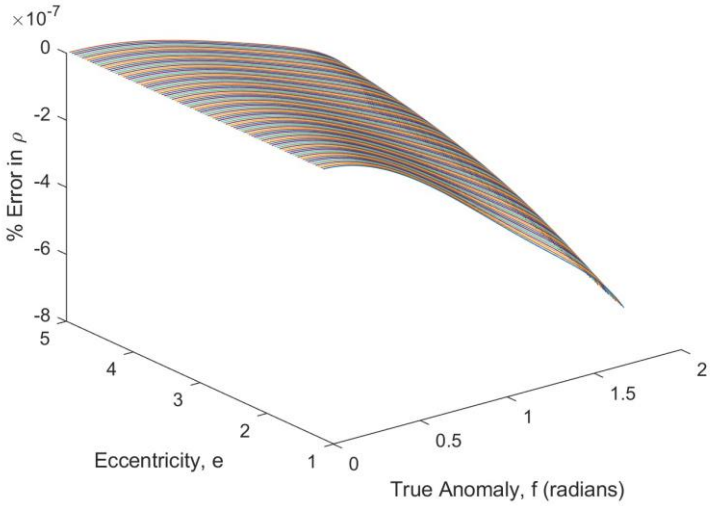


Figure 5-3: Error in ρ for Eccentricity-Anomaly Study

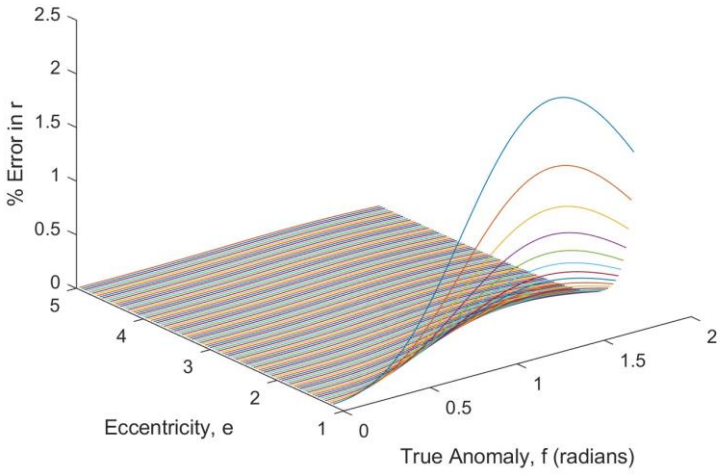


Figure 5-4: Error in Range for Eccentricity-Anomaly Study

Figs. 5-1 – 5-4 indicate accurate results along the defined eccentricity and true anomalies. The error in ρ is very close to zero and the range r maintains less than one percent error over a majority of the e-f range, the exception being close to e = 1.2 and f = 73 degrees. This likely is due to the lower eccentricities approaching parabolic nature. The peak error near f = 73 degrees

has no apparent physical significance. The most likely explanation is that this peak is an artifact of the second-order expansion solution, which contains nonlinear combinations of cosf and sinf. Increasing θ initially produces the highest amount of error; however, that drops to less than 10% for values above 80 degrees. An acceptable range of values for θ can be further shown in the expanded view of Fig. 5-2, which shows that error is drastically reduced for eccentricity greater than 1.4 and true anomaly greater than 23 degrees. Thus, the model is shown to produce very accurate results for a large range of eccentricities and true anomalies, which could prove useful when mission criteria require less computationally intensive approximations for inter-satellite range.

# Chapter 6

# Series Expansion Effect on Analytical Model

Once observations were made about the accuracy of the analytical model, a thorough study could be implemented to examine how adding a time-explicit series expansion of the hyperbolic anomaly H to the model affects the results.

## 6.1 Series Expansion Effect on Hyperbolic Anomaly

Before observing how the analytical model would be affected, the second- and third-order solutions dictated in Eqs. (4-9) and (4-10) needed to be studied against a numerical solution to hyperbolic anomaly when both solutions are time dependent. This was done using the same initial conditions. The eccentricity range was defined to be between 1.2 and 1.6 and the time span from 0 to 1 TU. Since both analytical approximations diverge faster as eccentricity becomes larger, the eccentricity range was limited so that the error would be kept to a reasonable order of magnitude. The second- and third-order error to the numerical solution are shown for 10 different values of e in Figs. 6-1 and 6-2.

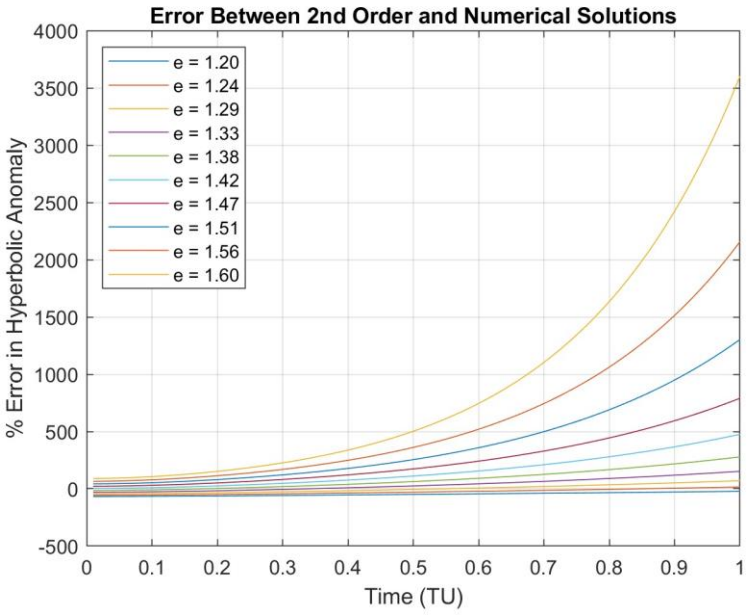


Figure 6-1**:** Error in 2nd Order Approximation of Hyperbolic Anomaly

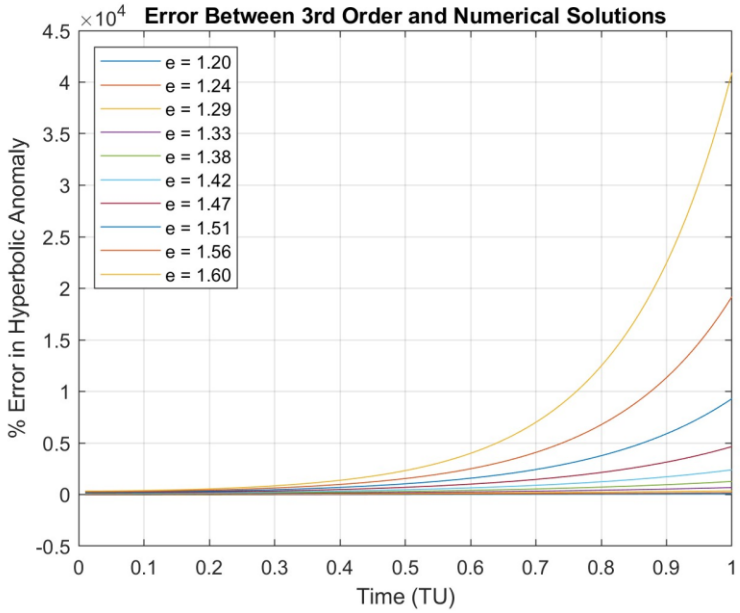


Figure 6-2**:** Error in 3rd Order Approximation of Hyperbolic Anomaly

From Fig. 6-1 and Fig. 6-2 it is clear that the third-order approximation produces a larger amount of error at a given eccentricity, especially as time increases. While third-order approximations may be acceptable for smaller time values and lower eccentricity, the second-

order solution seems to produce a wider range of values that could prove useful. This is likely due to the values of eccentricity being larger than one, which forces the system to diverge from a solution faster for third order than second order. These trends become clearer when the time span is reduced to the range 0 to 0.4 TU.

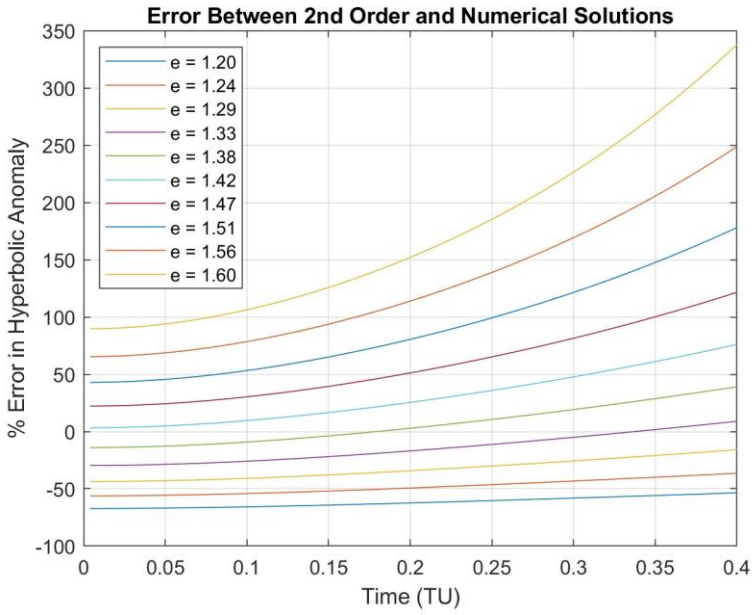


Figure 6-3: Adjusted Time Span for 2nd Order Approximation Error

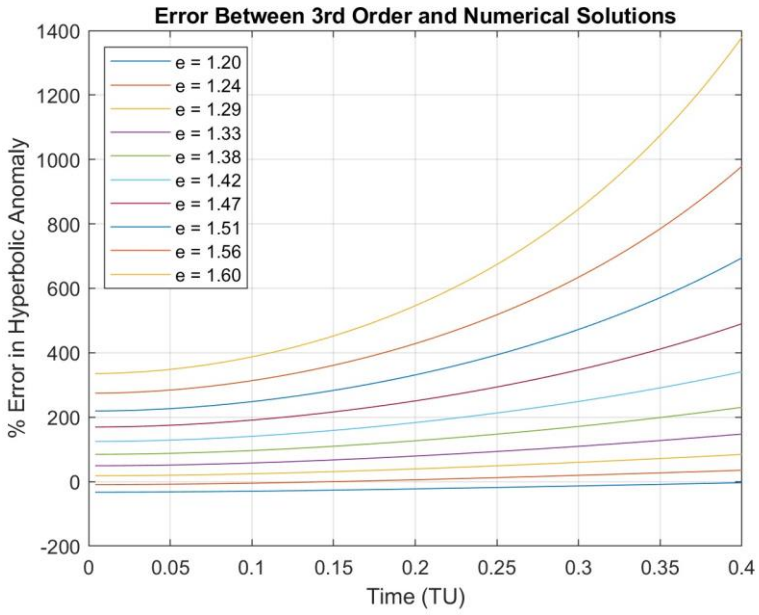


Figure 6-4: Adjusted Time Span for 3rd Order Approximation Error

After observing the reduced time range, the second-order solution continues to predict the actual hyperbolic anomaly much more accurately than the third-order solution.

This is further shown by plotting the second-order, third-order, and numerical solutions for the first and last values in the studied eccentricity range as seen in Figs. 6-5 and 6-6.

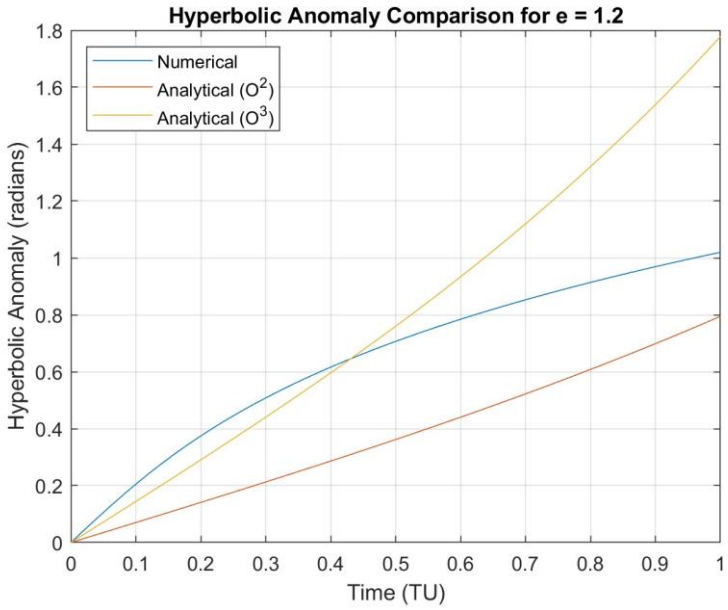


Figure 6-5: Comparing Hyperbolic Anomaly at e = 1.2

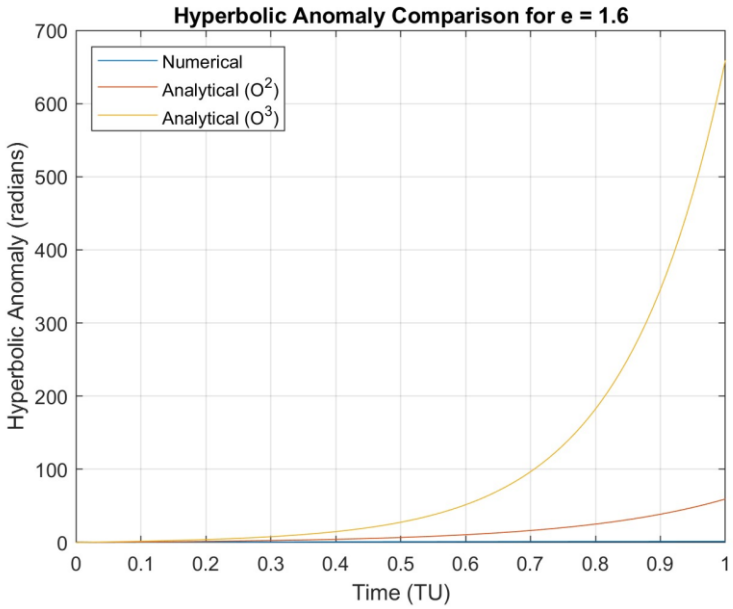


Figure 6-6: Comparing Hyperbolic Anomaly at e = 1.6

Fig. 6-5 shows that for lower values of time and eccentricity, the third-order solution can be more accurate than the second-order; however, as shown in Fig. 6-6, as time and eccentricity

increase the third-order solution becomes less accurate by a large margin. Thus, there is a fine limit on what the third-order solution would be able to accommodate.

In the second study, the conditions were refined to determine a range of values where the second-order solution could prove to be reasonably accurate.

## 6.2 Refining the Series Expansion Study

In order to find a range for reasonable accuracy of the second-order solution, different values for radius or periapsis were tested with various adjustments to the eccentricity range and time span. In performing this analysis, it was found that the second-order solution could have a reasonable match to the numerical solution when radius of periapsis was set to 3.2 LU, the eccentricity range was shortened to 1.4, and the time span was changed to 0 to 0.7 TU. The error graphs for second order and third order are depicted in Figs. 6-7 and 6-8.

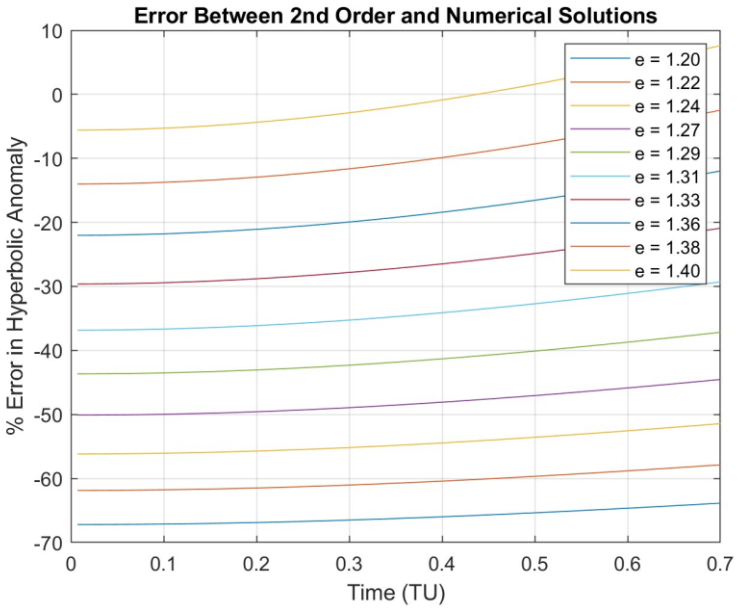


Figure 6-7: New Error in 2nd Order Approximation to Hyperbolic Anomaly

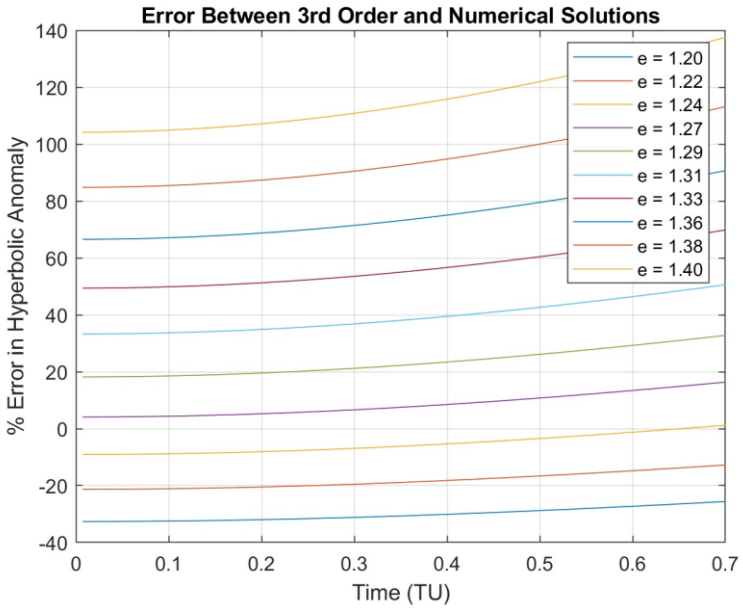


Figure 6-8: New Error in 3rd Order Approximation to Hyperbolic Anomaly

As seen in Figs. 6-7 and 6-8, by increasing radius of periapsis and adjusting the time and eccentricity ranges, reasonably accurate solutions for 2nd and 3rd order approximations can be discovered. Between eccentricity of 1.2 and 1.27, the 3rd order approximation can be found to be under 20% error from the numerical solution while between 1.36 to 1.40 eccentricity the 2nd order approximation can be found to be under 20% error. By examining the beginning and end of the range of eccentricities, the accuracy of the second order solution can be shown to decrease as eccentricity increases while the third order approximation increases across the entire range.

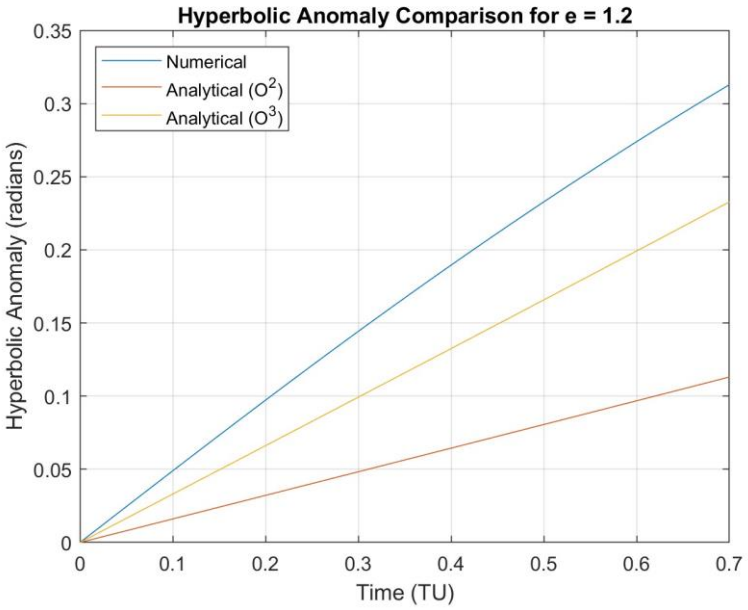


Figure 6-9: Comparing Hyperbolic Anomaly at e = 1.2

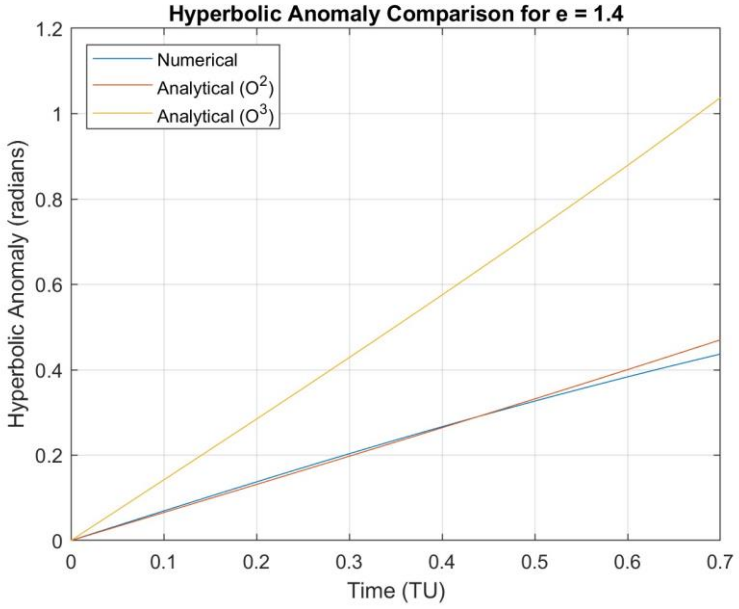


Figure 6-10**:** Comparing Hyperbolic Anomaly at e = 1.4

### 6.3 Expanded Trigonometric Function Error

Since most eccentricities recorded very high error for the hyperbolic anomaly expansion, another experiment was performed to examine how this generated error would respond to the application of sin(f), cos(f), and sin(2f). If the error could be decreased inside of these functions, then the application of the analytical solution could be applied as normal. Making use of relationships between trigonometric functions in f and H [10] yields

$$\sin f = \frac{\sqrt{e^2 - 1}\sinh H}{e\cosh H - 1}$$

$$\cos f = \frac{e - \cosh H}{e\cosh H - 1}$$

$$\sin 2f = 2\sin f \cos f \tag{6-1}$$

Lagrange's generalized expansion theorem Eq. (4-8) was applied to Eqs (6-1), with y = H, x = -N, $\alpha$ = e, and $\phi(x)$ = sinh(x). However, substituting Eqs. (6-1) into the second-order solution Eqs. (2-13) resulted in unbounded error for all values of e > 1. While this proved that it may not be feasible to directly apply Eq. (4-8) to Eq. (6-1), it allowed a narrower study to be conducted. Instead of applying equation (4-8), the already expanded hyperbolic anomaly was inserted into Eqs. (6-1) instead.

Thus, radius of periapsis was once again set to 1.2 LU with an eccentricity range from 1.2 to 3 and a time range from 0 to 5 TU. The results of this study for the third order approximation can be found in Figs. 6-11 – 6-13.

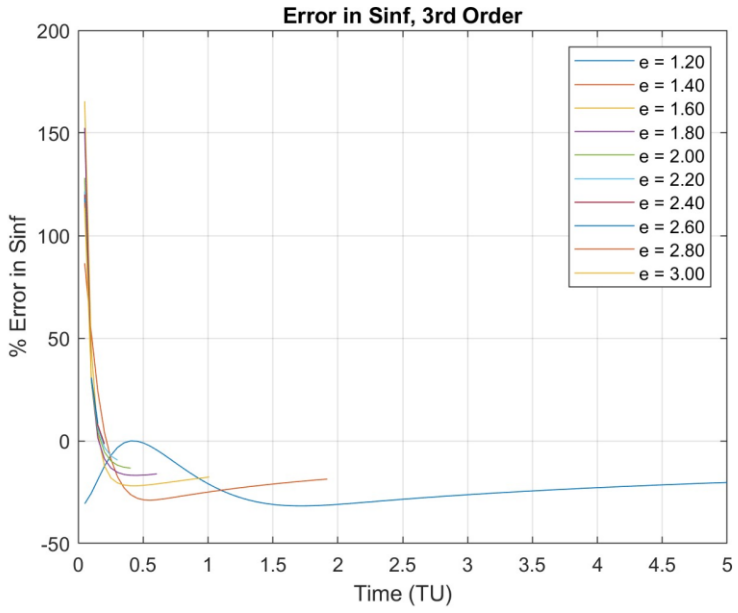


Figure 6-11: Error in 3rd Order Expansion of Sin(f) Function

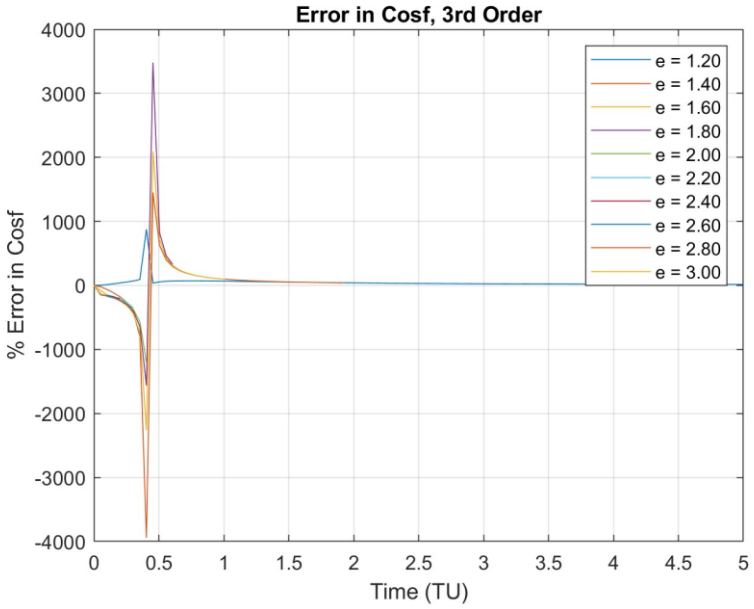


Figure 6-12: Error in 3rd Order Expansion of Cos(f) Function

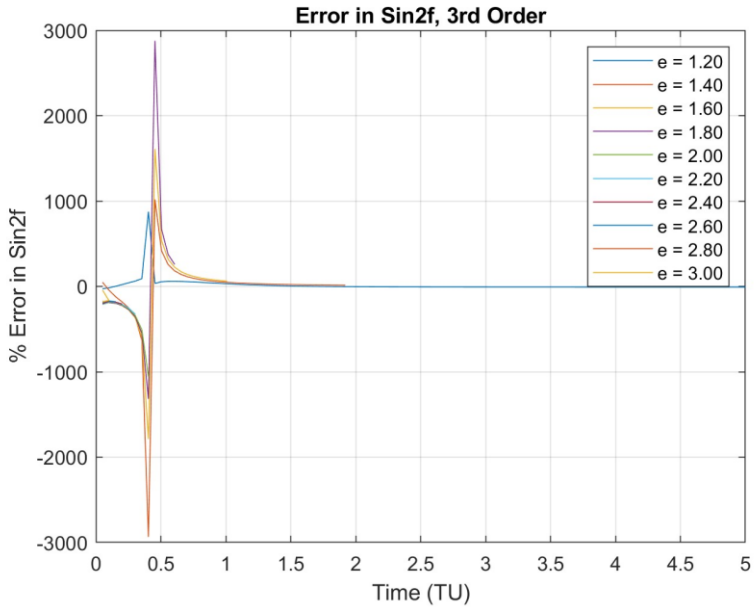


Figure 6-13: Error in 3rd Order Expansion of Sin(2f) Function

For the third order graphs, it seems that the sin(f) and sin(2f) functions can reduce some of the error between the approximation and the numerical solution. After about 1 TU the sin(2f) error can be reduced to under 40% for the 1.2 and 1.4 eccentricities while the sin(f) error never exceeds 40% after 0.5 TU. Unfortunately, there is still a very large oscillation in the sin(2f) and cos(f) functions at about 0.48 TU and large error for the entire time span for the cos(f) function. This results in the third order approximation not producing good enough results to be used in the analytical solution.

It is however interesting that error becomes extreme at 0.48 TU for the trigonometric functions. Since this is not a discontinuity or singularity for any of the functions, it is hard to say exactly what causes this error and could be useful to assess in a further study of this model.

Next, the same study was performed for the second order system.

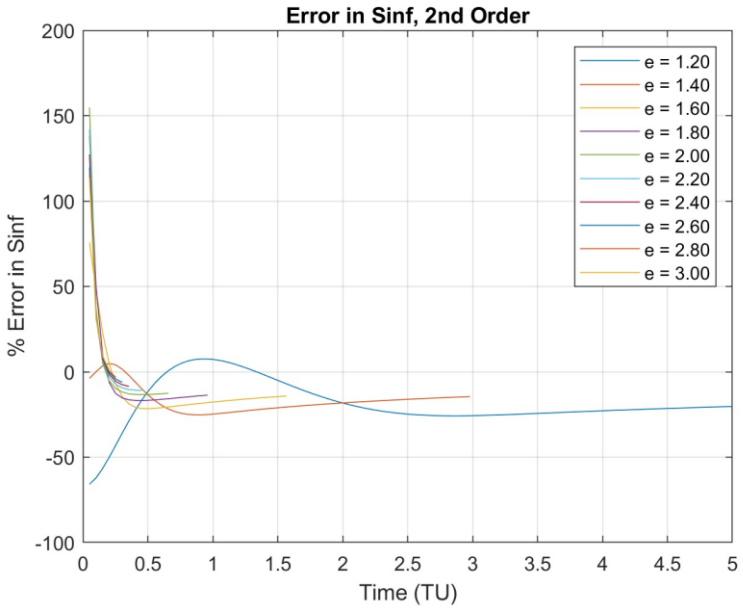


Figure 6-14: Error in 2nd Order Expansion of Sin(f) Function

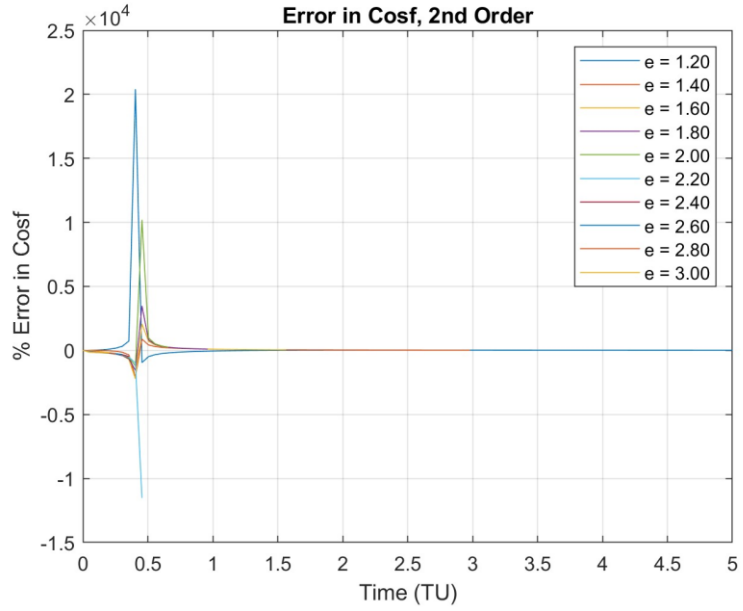


Figure 6-15: Error in 2nd Order Expansion of Cos(f) Function

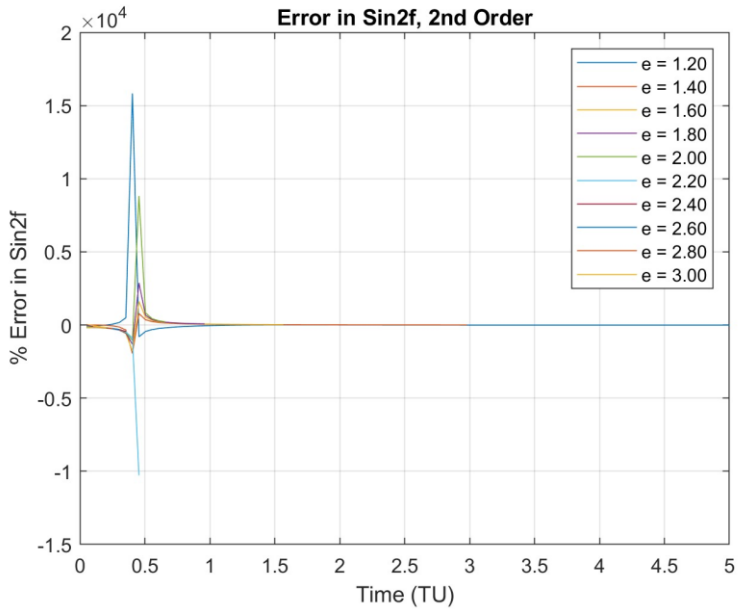


Figure 6-16: Error in 2nd Order Expansion of Sin(2f) Function

The error in the trigonometric functions is generally lower for the second order solution. The worst error stems from the cosine function, which maintains a high error until about 1.4 TU where error can be found to be less than 50% for the eccentricities that follow. Looking further down the time span, the error can be reduced to about 25% after around 1.56 TU. Likewise, sin(2f) follows a similar trend except the error is much less at all time units than the cosine function. In fact, the sin(2f) error drops below 10% after about 1.5 TU. Finally, while the error fluctuates for the sin(f) function, error is never more than 25% and it can be seen that the sin(f) function is quite accurate for most eccentricities between 0.25 and 0.5 TU.

## 6.4 Analytical Model Observations

Following the trigonometric error analysis, the time dependent model to the analytical relative motion solution could be assessed. To begin, a study over a time range of 0 to 3 TU and an eccentricity range of 1.2 to 3 with radius of periapsis set to 1.2 LU was performed.

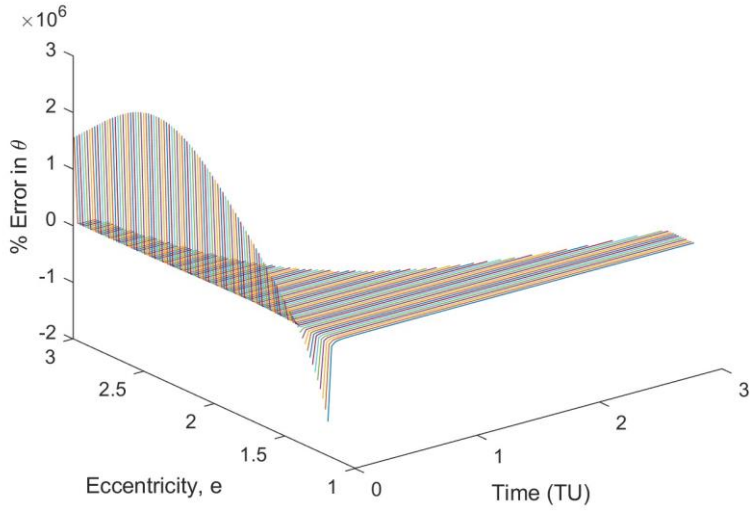


Figure 6-17: Error in θ for Time Dependent Study

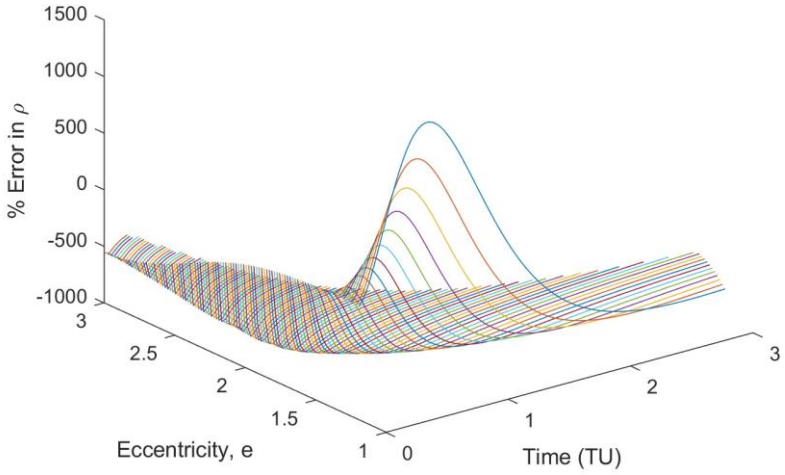


Figure 6-18: Error in ρ for Time Dependent Study

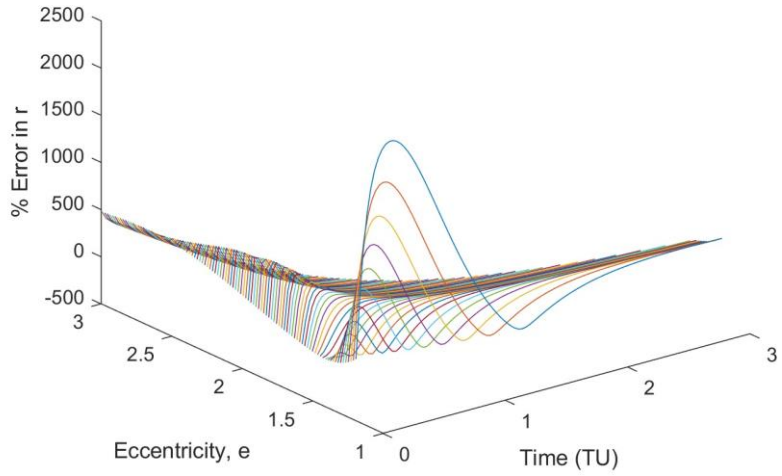


Figure 6-19: Error in Range for Time Dependent Study

As is shown, the error in these graphs increases drastically as time increases. This is most likely a direct result of the higher errors found inside the trigonometric error study. By having multiple instances of sin(f), cos(f), and sin(2f) in the analytical solution, error becomes compounded especially for the cos(f) function. This results in large inaccuracies in the calculation of the spherical coordinates. However, from the graphs, it appears as though at smaller values of time, more accurate approximations can be made. This is made clear by Fig. (6-20).

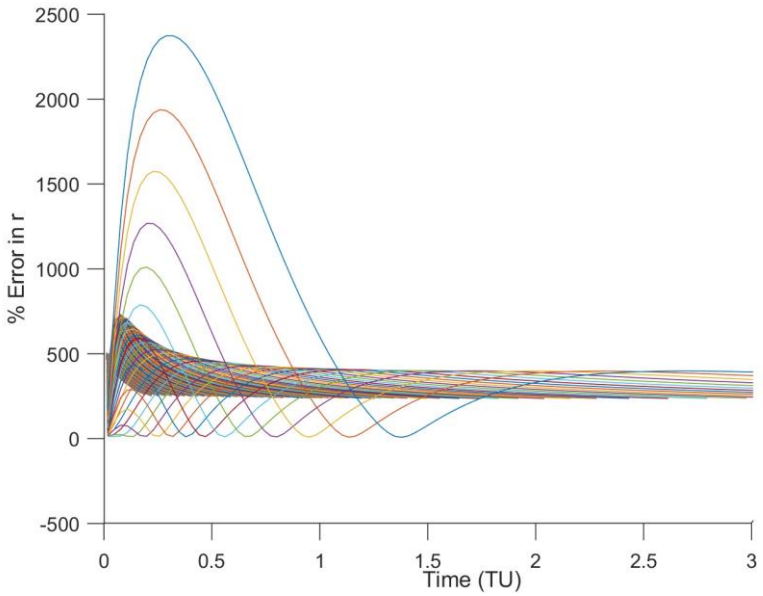


Figure 6-20: Side View of Range Error

Thus, to understand if range can be reduced and approximated better, the eccentricity and time range were updated. In Fig. (6-21), eccentricity was taken to be 1.4 to 3 and the time was spanned from 0 to 0.2 TU.

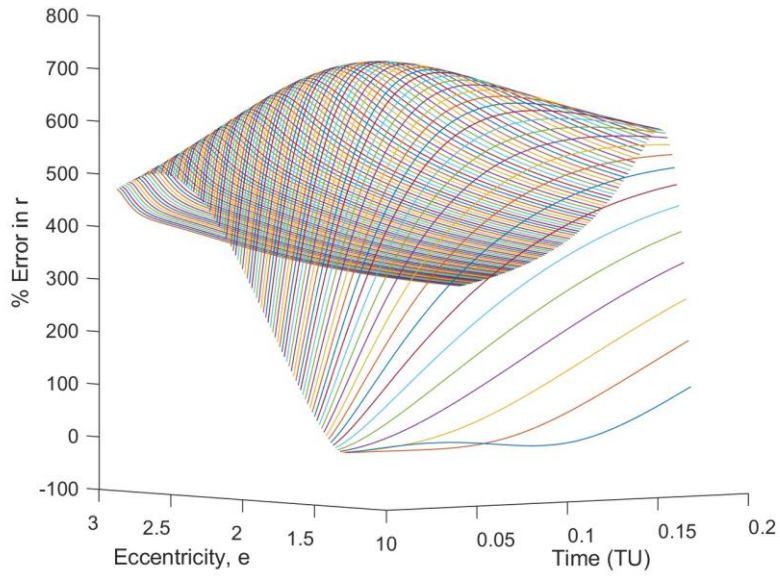


Figure 6-21: Error in Range with Adjusted Eccentricity and Time

By viewing the three-dimensional plot from a side view, it is clear that while error can be reduced by varying the parameters, the error in range is still too high to be useful in orbit calculations. Only specific values of eccentricity and time can be used to get a reasonable approximation between the range of two spacecraft. Thus, it is hard to find usefulness in the $2^{nd}$ order time-dependent approximation of the hyperbolic anomaly except for eccentricities of 1.4 and 1.41 before 0.15 TU.

# Chapter 7

# Conclusion

## 7.1 Summary

By applying a second-order approximate curvilinear solution to spacecraft on hyperbolic trajectories, the effective range and spherical coordinate error between two vehicles can be assessed. The resulting study found that by directly applying the model to eccentricities greater than one, very accurate results could be produced for the spherical coordinates as well as only 2.5% error to the numerical solution in range calculations.

A further study was conducted to examine the effects of adding a time-dependent expansion for hyperbolic anomaly to the analytical solution. Second- and third-order approximations were attempted, however, these models proved to be accurate only for certain values of radius of periapsis and eccentricity. To determine the range of usefulness for these models, the expansion of hyperbolic anomaly was compared to the numerical solution for a wide range of time and eccentricities. The radius of periapsis was then adjusted to determine at what value error could be minimized.

This time-dependent approach was examined further by direct expansion of the trigonometric terms in the analytical approximation. The results of this experiment showed that as time was increased, the trigonometric terms could become more accurate. However, these results were still mostly over 25% error, which contributed to the large resulting error present in the application of the expansion to the analytical solution. The biggest contributor being the cosine function, which always maintained an error larger than about 20%.

Finally, when the hyperbolic anomaly expansion was applied to the analytical solution to create a time-dependent approximate solution, the error was found to drastically increase as time increased. The time and eccentricity were then adjusted to examine what the error would look like on a smaller time scale and a slightly larger starting eccentricity. This produced figures with less error, but only specific values of eccentricity and time could prove useful in missions that require precise orbit calculations between two spacecraft. As such, even though there are specific values where this type of analytical model could be applied, the overall expansion of the hyperbolic anomaly will not be accurate enough to produce useful results over a wide range of values of time and eccentricity along an orbit.

## 7.2 Future Scope

Future work should examine other means to achieve the goal of a feasible time-explicit approximation for relative motion on hyperbolic orbits. Possible methods include the use of series reversion applied to the hyperbolic trigonometric functions or the use of series expansions in inverse powers of eccentricity.

The non-time-dependent solution has been shown to give a good approximation and further work making use of that could examine the problem of finding a suitable satellite geometry for distributed sensing. An optimizer for minimizing the average range-rate for some specified range between spacecraft pairs could be implemented to determine a way that multiple objects on different orbits can find a time to communicate with each other while they move together near a planet. This would entail the use of a multi-objective optimization algorithm, with the objectives being the range-rates of the spacecraft pairs.

Finally, a further study of this model as it applies to the range-rate should also be explored. Differentiating the range, as approximated by the non-time-dependent solution, can be

transformed to a time-derivative, i.e. range-rate. In parallel, the time-dependent approximation could be directly differentiated. Although that approximation shows poor performance for approximating range, it could conceivably yield acceptable results for range-rate. A distributed-sensor system could then make use of one model for approximating range and another for range-rate.

# REFERENCES

[1] Barnhart, D., Vladimirova, T., and Sweeting, M. “Enabling Space Sensor Networks with PCBSat,” University of Surrey, 2007.

[2] Edlerman, E., Gurfil, P. “Cluster-Keeping Algorithms for the Satellite Swarm Sensor Network Project,” Journal of Spacecraft and Rockets, Vol. 56, No. 3, 2019, doi: 10.2514/1.A34151

[3] Dubois, A. “Formation Flying.” NASA, NASA, 28 July 2021, https://www.nasa.gov/centers/ames/engineering/divisions/spaceflight/flight-dynamics/formation-flying.

[4] Takahashi, Y. and Scheeres, D.J. "Small-Body Postrendezvous Characterization via Slow Hyperbolic Flybys," Journal of Guidance, Control, and Dynamics, 2011. 34(6): p. 1815-1827.

[5] Crowe, W., Kinkaid, N., Olsen, J., and Page, J., "Spacecraft Swarm Positioning During Asteroid Flybys Using Relative Doppler and Ranging," AIAA/AAS Astrodynamics Specialist Conference, 13-16 September 2016, Long Beach, California, doi: 10.2514/6.2016-5516

[6] Stueck, C. “Investigation of the Relative Motion Between Spacecraft on Different Hyperbolic Trajectories,” B.S. honors thesis, The Pennsylvania State University, 2022.

[7] Sullivan, J., Grimberg, S. and D’Amico, S. “Comprehensive Survey and Assessment of Spacecraft Relative Motion Dynamics Models,” Journal of Guidance, Control, and Dynamics, Vol. 40, No. 8, 2017, pp. 1837-1859, doi: 10.2514/1.G002309

[8] Willis, M., Alfriend, K.T., and D'Amico, S. "Second-order solution for relative motion on eccentric orbits in curvilinear coordinates," Advances in the Astronautical Sciences, Vol. 171, 2020, pp. 767- 790.

[9] Prussing, J.E. and Conway, B.A., Orbital Mechanics, 2nd ed., Oxford University Press, New York – Oxford, 2013.

[10] Battin, Richard H. An Introduction to the Mathematics and Methods of Astrodynamics; Revised Edition. AIAA, 1999.

[11] K. Yamanaka and F. Ankersen, "New State Transition Matrix for Relative Motion on an Arbitrary Elliptical Orbit," Journal of Guidance, Control, and Dynamics, Vol. 25, No. 1, 2002, pp. 60–66

[12] Vasile, M., "A Global Approach to Optimal Space Trajectory Design," Advances in Astronautical Sciences, Vol. 114, 2003, pp. 621-640.

[13] Melton, R. G. "Relative Motion Between Hyperbolic Trajectories -- A Technical Footnote ," International Astronautical Congress, September 18-22, 2022, Paris, France, paper IAC-22,LBA,C1,1,x74549.

[14] Xie, K., Liang, F., Xia, Q., Wang, N., Yuan, H., Liu, X., Wu, Z. "Power Generation on a Bare Electrodynamic Tether During Debris Mitigation in Space," Beijing Institute of Technology, 2021.

[15] Kluever, C. "Spaceflight Mechanics," Encyclopedia of Physical Science and Technology, Vol. 3, 2003, pp. 507-520.

[16] Tapley, B. D., Schutz, B., Born, G. Statistical Orbit Determination. Burlington, MA: Elsevier Academic Press, 2004. 41

[17] Vallado, D.A., Fundamentals of Astrodynamics and Applications, 2 nd ed. El Segundo, CA: Microcosm Press, 2001.

[18] Wu, C., Curlander, J. C., and di Cenzo, A., “Determination of spacecraft attitude using synthetic aperture radar data” American Institute of Aeronautics and Astronautics, Inc., 1980, p. 57-60.

[19] Chung, S., Hadaegh, F. Y., Swarms of Femtosats for Synthetic Aperture Applications. In: 4th international conference on spacecraft formation flying missions and technologies (SFFMT), May 18-20, 2011, St. Hubert, Quebec.

[20] Boyce, William E., and Richard C. DiPrima. Introduction to Differential Equations: Wiley, New York, 1970.

[21] Mathworks, ODE45 Documentation. [Online] Available: https://www.mathworks.com/help/matlab/ref/ode45.html